Numerical study of the wrinkling of a stretched thin sheet

Tae-Yeon Kim [a], Eric Puntel [b], Eliot Fried [a,*]

[a] Department of Mechanical Engineering, McGill University, Montréal, Québec, Canada H3A 2K6
[b] Dipartimento di Ingegneria Civile e Architettura, Università di Udine, via Cotonificio 114, 33100 Udine, Italy

ARTICLE INFO

ABSTRACT

A thin sheet clamped at opposite ends and stretched develops wrinkles parallel to the direction of the applied tensile strain due to the hindered Poisson lateral contraction at the clamps. To study this phenomenon, a variational model recently proposed by Puntel, Deseri and Fried is adopted. The relevant energy functional includes bending and membranal contributions and is minimized subject to a constraint on the area of the mid-surface of the sheet. A fourth order partial-differential equation is henceforth obtained and numerically implemented using B-splines. Predictions are obtained concerning the number of wrinkles, critical applied stretches, and scaling relationships for wrinkle amplitude and wavelength. Both a linearized version of the boundary-value problem based on the small-slope approximation and a fully nonlinear one are considered: their results are found to be in good agreement for the whole range of applied stretches taken into account. Comparisons with previous analytical results by Puntel, Deseri and Fried, who used different boundary conditions and an Ansatz on the deflection function are also provided. The numerical results substantially confirm the validity of the analytical predictions. The present work provides then an alternative numerical method for the study of wrinkling in thin sheets and supports the use of analytical and semi-analytical solutions as viable options for specific geometries. Though further investigation, particularly experimental, is still needed, extensive comparisons of the results with other studies available in the literature provide confirmation for the scaling laws and signal that predicted values of the critical stretches may only be accurate for higher length-to-width aspect ratios.

1. Introduction

Wrinkles arise in thin sheet subject to in-plane loading as manifestations of instability due to the almost negligible flexural stiffness of membranes and the associated inability to withstand compressive loading.

In general, a membrane subject to in-plane loading involving a combination of shear and tension will generally exhibit taut, wrinkled, and slack zones. In taut zones, the in-plane principal stresses are tensile. In wrinkled zones, one of the in-plane stresses vanishes and the crests and troughs of the wrinkles are roughly parallel to trajectories of nonvanishing tension. In slack zones, which do not appear in the absence of wrinkles, the in-plane principal stresses both vanish.

Wrinkles have traditionally and firstly been a matter of concern in the aerospace industry for their negative impact on the performance and longevity of thin structural elements. To avoid wrinkles and to apply tension as uniformly as possible throughout the membrane surface, compensating supports such as pillars and arches are introduced or cables are attached to the edges and interior of

the membrane. This solution is not always feasible because it involves often unwelcome weight increases and because larger tensile stresses can intensify risks of material creep, crack initiation and propagation, and failure. When otherwise wrinkles can or have to be accounted for, the stress distribution changes significantly and can be computed resorting to tension-field theory (see e.g. Steigmann, 1990). Albeit elegant and mathematically sound, this theory neglects the bending stiffness of the membrane and assumes wrinkles of infinitesimal amplitude and wavelength. It is therefore not helpful when aiming at characterizing wrinkles. This can occur, as observed by Jenkins et al. (1999), when attempting to ensure that precision requirements of space reflector antennas are met.

Leaving aside aerospace applications, there are several other areas in which quantitative assessment of wrinkling is of current importance. In the steel lamination industry different wrinkling patterns occur during rolling and leveling, i.e. straightening by stretching, of thin metal strips. Differences in the distribution of plastic strains along the width of the strip are inferred from the observation of wrinkles (Fischer et al., 2000). The analytical and numerical work by Fischer et al. (2000) is also relevant for the similarity of the problem studied therein with the one investigated here. In the medical field, there is a need for wound and burn

* Corresponding author. Tel.: +1 514 398 3739.
  E-mail address: eliot.fried@mcgill.ca (E. Fried).

treatments (Hudson and Renshaw, 2006) and for surgical techniques that ensure proper circulation, mobility and minimal scarring subsequent to healing (Lott-Crumpler and Chaudhry, 2001; Georgeu and Ross, 2002; Cerda, 2005; Hofer and Mureau, 2009; Ueda et al., 2009). Optical measurements of wrinkles on thin polymer films might provide a simple and accurate alternative to more traditional techniques used to determine thicknesses, mechanical properties (Stafford et al., 2004), and residual stresses (Chung et al., 2009). Similarly, measuring wrinkles created by cells crawling on thin silicone substrates might provide important insight regarding cell locomotion (Burton and Taylor, 1997; Harris et al., 1980). Applications that exploit wrinkling to tune the optical properties of cavities (Kolaric et al., 2010) and to shape capillaries for micro-fluidic purposes (Ohzono et al., 2009) also seem relevant.

The first numerical approaches to wrinkling were based on membrane elements and tension-field theory. One such approach, called *Iterative Material Properties* (IMP), was initially developed by Miller and Hedgepeth (1982) and subsequently by Miller et al. (1985). An iteratively and element-wisely varying Poisson's ratio is introduced to model the geometric strain in the direction perpendicular to the wrinkles. In this approach, an ad hoc *wrinkling criterion* based on the combined evaluation of the sign of the principal stresses and strains is used to activate the modified material properties.

Other tension-field theory approaches using membrane elements are based on iterative no-compression models devised by Contri and Schrefler (1988).

Liu et al. (2000) employed the tension-field theory solution obtained using membrane elements to derive information on actual wrinkling patterns via semi-analytical determination of impeding buckling modes.

In general, however, shell elements are preferred when aiming at the qualitative characterization of wrinkles. The first to employ three-dimensional shell elements to this end were Tomita and Shindo (1988). A common trait to studies adopting shell elements is the application of suitable imperfections to trigger the out-of-plane deflection modes when starting from an in-plane stretched membranal configuration. Wong and Pellegrino (2006c) used preliminarily extracted eigenmodes of the tangent stiffness matrix as initial imperfections. Other alternatives include randomly distributed out-of-plane imperfections, as proposed by Tessler et al. (2005), and the application of small forces perpendicular to the membrane, as advocated by Leifer and Belvin (2003).

The present study was motivated by the experimental and analytical work of Cerda et al. (2002) and Cerda and Mahadevan (2003). In their experiment, a polyethylene thin sheet of rectangular shape is clamped along two opposite edges and stretched. As a result of the hindered Poisson contraction occurring near the fixed ends, a zone of in-plane compressive stresses forms and wrinkling ensues. An effective depiction of this phenomenon can be found in Friedl et al. (2000). Cerda et al. (2002) measured the wavelength, but not the amplitude, of the wrinkles and the corresponding stretch at which they occurred.

The analytical part of Cerda, Ravi-Chandar and Mahadevan's work has two distinguishing features. The first distinguishing feature lies in the energy functional that is minimized to solve the boundary-value problem for the stretched thin sheet. In addition to terms that can be likened to membranal and Föppl–von Kármán bending energy contributions, a geometric constraint on the length of the sheet in the direction perpendicular to the direction of stretch is introduced. Cerda, Ravi-Chandar and Mahadevan consider pinned boundary conditions at the clamped ends which do not reproduce the hindered Poisson contraction effect. Hence, the pre-stretch of the thin sheet is a homogeneous uniaxial tension. For this reason, the geometric constraint is precisely an ad hoc measure that forces the thin sheet to explore out-of-plane

wrinkled configurations afar from the otherwise stable flat solution. The second distinguishing feature is an educated guess regarding the structure of the deflected solution. Specifically, it is assumed to be a half-sinusoid in the direction of stretch and a sinusoid depending on three parameters, namely amplitude, wavelength and phase, in the direction perpendicular to the direction of stretch. Minimizing of the constrained energy functional yields scaling relations for the amplitude and wavelength of wrinkles as functions of the applied stretch. The former scaling relation fits well with the experimental data. No critical values of the applied stretch associated with the onset of wrinkled configurations are provided.

In a recent paper, Puntel et al. (2011) reconsider the work of Cerda, Ravi-Chandar and Mahadevan. Both the variational framework and the pinned boundary conditions used in that work are retained. However, each term of the energy functional is revised. The geometric constraint is relaxed by prescribing the area of the mid-surface of the sheet. Membranal and bending energy terms are properly derived from kinematical assumptions. Moreover, no Ansatz is made for the deflection in the direction perpendicular to the direction of stretch. Minimization of the energy functional leads to a differential Euler–Lagrange equation and no longer to a set of algebraic equations. To solve the problem analytically, the Euler–Lagrange equation is further linearized according to a small-slope approximation.

Numerous results are obtained on this basis. First, a sequence of values of applied stretch is determined, each corresponding to the onset of a configuration with a different number of wrinkles. Second, wrinkle amplitude and wavelength are expressed as functions of the applied stretch. For sufficiently large values of the applied stretch, the scaling relations obtained by Cerda et al. (2002) are recovered. Finally, wrinkles are found to have unequal amplitude in the direction perpendicular to the applied stretch, namely decreasing in a semi-sinusoidal fashion from the center of the sheet towards the free edges.

The present study constitutes a numerical counterpart of the paper of Puntel et al. (2011). Its main aim is to remove several of the simplifying assumptions motivated by the analytical treatment, thus obtaining improved solutions and allowing for an assessment of the validity range of the simplifications imposed previously. In particular, fixed, in contrast to pinned, boundary conditions are imposed at the fixed edges. Moreover, at the free edges, exact traction-free boundary conditions are used instead of phenomenological ones. Of course, no a priori Ansatz is adopted for the deflection. Two different cases are investigated: one in which the small-slope approximation, which enables the linearization of the Euler–Lagrange equation, is retained and one in which it is removed. In either case, the geometric constraint is nonlinear and iterative solution schemes are required. A finite-element code, based on B-splines, has been developed specifically for this study together with the weak formulation of the variational problem and the tangent stiffness matrix for the Newton–Raphson algorithm. The main outcome of the analyses is that, despite the several simplifications removed, for the specific geometry considered the analytical results obtained more directly by Puntel et al. (2011) are essentially still valid. The present work provides then an alternative numerical method for the study of wrinkling in thin sheets and supports the use of analytical and semi-analytical solutions as viable options for specific geometries. Though further investigation, particularly experimental, is still needed, extensive comparisons of the results with other studies available in the literature provide confirmation for the scaling laws and signal that predicted values of the critical stretches may only be accurate for higher length-to-width aspect ratios.

The paper is structured as follows. In Section 2, the boundary-value problem is formulated. In Section 3, the results of the work of Puntel et al. (2011) are summarized. In Section 4, the role of the geometric constraint in the variational formulation is discussed.

In Sections 5 and 6, the weak formulation of the variational problem and its finite-element discretization are introduced. In Section 7, insight concerning the derivation of the consistent tangent stiffness matrix employed in the full Newton–Raphson method is provided. The numerical analyses and results are described and discussed in Section 8. Finally, in Section 9, detailed comparisons with other studies available in the literature are provided.

2. Problem description

Consider a rectangular sheet of length $2L_1$, width $2L_2$, and thickness h. Choose a positively-oriented, orthonormal basis $\{\mathbf{e}_1, \mathbf{e}_2, \mathbf{e}_3\}$ with associated Cartesian coordinates x_1, x_2, and x_3 such that

$$-L_1 \leqslant x_1 \leqslant L_1, \quad -L_2 \leqslant x_2 \leqslant L_2, \quad -\frac{1}{2}h \leqslant x_3 \leqslant \frac{1}{2}h. \tag{1}$$

The mid-surface of the sheet is denoted by $\Omega = (-L_1, L_1) \times (-L_2, L_2)$ and its boundary is denoted by $\partial\Omega$. For later reference, the boundary $\partial\Omega$ is subdivided into two parts

$$\partial\Omega_{\text{fxd}} := \{(x_1, x_2) : x_1 = \pm L_1, \ -L_2 \leqslant x_2 \leqslant L_2\}, \tag{2}$$

$$\partial\Omega_{\text{free}} := \{(x_1, x_2) : x_2 = \pm L_2, \ -L_1 \leqslant x_1 \leqslant L_1\}, \tag{3}$$

where different boundary conditions are applied. The outer normal of $\partial\Omega$, lying in plane $x_3 = 0$, is denoted by $\mathbf{n}$ and the counterclockwise tangent vector to the boundary is denoted by $\mathbf{t}$.

Motivated by the experiments of Cerda et al. (2002), suppose that the $x_1 = \pm L_1$ edges of the sheet are subject to uniform displacements

$$\mathbf{u}(\pm L_1, x_2, x_3) = \pm \varepsilon L_1 \mathbf{e}_1, \quad -L_2 \leqslant x_2 \leqslant L_2, \quad -\frac{1}{2}h \leqslant x_3 \leqslant \frac{1}{2}h \tag{4}$$

with $\varepsilon > 0$. Away from these edges, a homogeneous pre-stretch displacement field $\bar{\mathbf{u}}$ satisfying

$$\bar{\mathbf{u}}(x_1, x_2, x_3) = \varepsilon x_1 \mathbf{e}_1 - v\varepsilon(x_2\mathbf{e}_2 + x_3\mathbf{e}_3) \tag{5}$$

is assumed.

To study the occurrence of wrinkles in the stretched sheet, an energy functional

$$\mathcal{U} = \mathcal{F}^{\text{b}} + \mathcal{F}^{\text{m}} - \varepsilon^* \mathcal{T} \tag{6}$$

is considered. The term

$$\mathcal{F}^{\text{b}} = \frac{B}{2} \int_\Omega [w_{,\alpha\alpha} w_{,\beta\beta} - (1 - v)(w_{,\alpha\alpha} w_{,\beta\beta} - w_{,\alpha\beta} w_{,\alpha\beta})] da \tag{7}$$

indicates the Kirchhoff–Love bending energy,[1] where w is the deflection in the $\mathbf{e}_3$-direction and the bending stiffness B is given in terms of Young's modulus E, Poisson's ratio v, and the sheet thickness h by

$$B = \frac{Eh^3}{12(1 - v^2)}.$$

The membranal energy term $\mathcal{F}^{\text{m}}$, which includes contributions from the pre-stretch $\bar{\mathbf{u}}$ in (5) and, via a Föppl–von Kármán approximation, from the deflection w, has the form

$$\mathcal{F}^{\text{m}} = \frac{Eh}{2} \int_\Omega \left(\varepsilon^2 + \varepsilon w_{,1}^2 + \frac{1}{4b}(w_{,\alpha} w_{,\alpha})^2 \right) da, \tag{8}$$

where the coefficient b is given by

$$b = \frac{(1 + v)(1 - 2v)}{1 - v}.$$

Details of the derivation of (8) are provided by Puntel et al. (2011).

The last addend on the right-hand side of Eq. (6) consists of the Lagrange multiplier ε^* and the geometrical constraint,

$$\mathcal{T} = Eh \int_\Omega (\sqrt{1 + w_{,\alpha} w_{,\alpha}} - 1 - \varepsilon g(v, \varepsilon)) da, \tag{9}$$

which prescribes an assigned value $4L_1 L_2(1 + \varepsilon g(v, \varepsilon))$ to the area of the mid-surface of the sheet in the wrinkled configuration.

Taking the first variation of functional $\mathcal{U}$, the governing Euler–Lagrange equation

$$Bw_{,\alpha\alpha\beta\beta} - \frac{Eh}{2b}(w_{,\beta} w_{,\beta} w_{,\alpha})_{,\alpha} - Eh\varepsilon w_{,11}$$
$$+ Eh\varepsilon^* \left(\frac{w_{,\alpha}}{\sqrt{1 + w_{,\beta} w_{,\beta}}} \right)_{,\alpha} = 0 \tag{10}$$

is derived along with variationally consistent boundary conditions.

The deflection w and the normal rotation $w_{,n}$ are prescribed to be zero along the fixed edges

$$w = w_{,n} = 0 \quad \text{on } \partial\Omega_{\text{fxd}}, \tag{11}$$

while the bending moment and the generalized shear force are assigned along the free edges

$$B_M[w] = B_Q[w] = 0 \quad \text{on } \partial\Omega_{\text{free}} \tag{12}$$

with

$$B_M[w] := B(w_{,\alpha\alpha} - (1 - v)w_{,tt}), \tag{13}$$

and

$$B_Q[w] := -B((w_{,\alpha\alpha})_{,n} + (1 - v)w_{,ttn})$$
$$- Eh\varepsilon^* \frac{w_{,\alpha} n_\alpha}{\sqrt{1 + w_{,\beta} w_{,\beta}}} + \frac{Eh}{2}\left(2\varepsilon w_{,1} n_1 + \frac{1}{b} w_{,\beta} w_{,\beta} w_{,\alpha} n_\alpha\right). \tag{14}$$

2.1. Linearization based on the small-slope approximation

On invoking the classical small-slope approximation,

$$w_{,\alpha} w_{,\alpha} \ll 1, \tag{15}$$

the functionals $\mathcal{F}^{\text{m}}$ and $\mathcal{T}$ retain only terms up to the quadratic order and are replaced by $\mathcal{F}^{\text{m}}_{\text{lin}}$

$$\mathcal{F}^{\text{m}}_{\text{lin}} = \frac{Eh}{2} \int_\Omega (\varepsilon^2 + \varepsilon w_{,1} w_{,1}) da, \tag{16}$$

and $\mathcal{T}_{\text{lin}}$ respectively

$$\mathcal{T}_{\text{lin}} = Eh \int_\Omega \left(\frac{1}{2} w_{,\alpha} w_{,\alpha} - \varepsilon g(v, \varepsilon) \right) da. \tag{17}$$

As a result, the functional $\mathcal{U}$ defined in (6) becomes

$$\mathcal{U}_{\text{lin}} = \mathcal{F}^{\text{b}} + \mathcal{F}^{\text{m}}_{\text{lin}} - \varepsilon^* \mathcal{T}_{\text{lin}}. \tag{18}$$

The Euler–Lagrange equation obtained by taking the first variation of $\mathcal{U}_{\text{lin}}$ is now linear and reads

$$Bw_{,\alpha\alpha\beta\beta} - Eh\varepsilon w_{,11} + Eh\varepsilon^* w_{,\alpha\alpha} = 0. \tag{19}$$

The associated boundary conditions replacing (11) and (12) are

$$w = w_{,n} = 0, \quad \text{on } \partial\Omega_{\text{fxd}}, \tag{20}$$

$$B_M[w] = B_{Q\text{lin}}[w] = 0, \quad \text{on } \partial\Omega_{\text{free}}, \tag{21}$$

with

$$B_{Q\text{lin}}[w] := -B((w_{,\alpha\alpha})_{,n} + (1 - v)w_{,ttn}) - Eh\varepsilon^* w_{,\alpha} n_\alpha + Eh\varepsilon w_{,1} n_1. \tag{22}$$

3. The analytical results by Puntel et al. (2011)

This section summarizes the results obtained by Puntel et al. (2011) for easier comparison with the numerical results. The reader is addressed to the original work for an extensive description.

The analytical results of Puntel et al. (2011) are based on two main additional simplifications. The first is an Ansatz on the deflection w of the form

$$w(x_1, x_2) = \cos\left(\frac{\pi x_1}{2L_1}\right) y(x_2) \tag{23}$$

with y to be determined and $\cos(\pi x_1/2L_1)$ being the first buckling mode for a compressed beam pinned at its ends.

The second concerns the boundary conditions:

$$w = B_M[w] = 0, \quad \text{on } \partial\Omega_{\text{fxd}}, \tag{24}$$
$$w_{,n} = w_{,nn} = 0, \quad \text{on } \partial\Omega_{\text{free}}. \tag{25}$$

Despite what the subscripts in $\partial\Omega_{\text{fxd}}$ and $\partial\Omega_{\text{free}}$ suggest, along the edges where the stretch is applied, (24) imposes pinned instead of fixed boundary conditions and along the free edges (25) prescribes the slope and curvature in the x_2-direction normal to the edge to be zero. This latter condition is motivated on phenomenological grounds based on limited photographic account of the experiments of Cerda et al. (2002).

Substitution of (23) in (19) leads to a fourth order ordinary differential equation in y,

$$y_{,2222} + \left(\frac{\pi}{2L_1}\right)^2 e^* y_{,22} + \left(\frac{\pi}{2L_1}\right)^4 (e - e^*) y = 0 \tag{26}$$

to be satisfied on $(-L_2, L_2)$. This equation is formally identical to that governing the buckling of a beam on an elastic foundation. As for the boundary conditions, only prescriptions (25) applied along the free edges, aptly expressed in terms of y, remain:

$$y_{,2}(\pm L_2) = y_{,22}(\pm L_2) = 0. \tag{27}$$

The symbols e and e^* with $0 \leqslant e^* < e$ introduced in (26) stand for relative values of the applied stretch ε and Lagrange multiplier ε^* respectively:

$$e = \frac{\varepsilon - \bar{\varepsilon}}{\bar{\varepsilon}}, \quad e^* = \frac{\varepsilon^* - 2\,\bar{\varepsilon}}{\bar{\varepsilon}}, \quad \text{with } \bar{\varepsilon} = \left(\frac{\pi}{2L_1}\right)^2 \frac{h^2}{12(1-\nu^2)}. \tag{28}$$

After excluding two other possible solution regimes, the general solution is found to be of the form

$$\frac{y(x_2)}{2L_2} = \hat{A}\cos\left(\kappa_-\frac{\pi x_2}{2L_2}\right) + \hat{B}\sin\left(\kappa_-\frac{\pi x_2}{2L_2}\right) + \hat{C}\sin\left(\kappa_+\frac{\pi x_2}{2L_2}\right)$$
$$+ \hat{D}\cos\left(\kappa_+\frac{\pi x_2}{2L_2}\right) \tag{29}$$

characterized by two wavenumbers κ_+ and κ_- with $\kappa_+ > \kappa_- > 0$. The integration constants $\hat{A}$, $\hat{B}$, $\hat{C}$, $\hat{D}$ are determined from the boundary conditions (27) and give rise to a homogeneous linear system of equations. Non-trivial solutions for $\hat{A}$, $\hat{B}$, $\hat{C}$, $\hat{D}$ are possible when the rank of the coefficient matrix of that linear system is not full. For this to occur, it is found that either one of these two conditions

$$\mathcal{F}^+(\kappa_+, \kappa_-) := \frac{\pi}{2}\kappa_+\sin\left(\frac{\pi}{2}\kappa_+\right)\cos\left(\frac{\pi}{2}\kappa_-\right)$$
$$- \frac{\pi}{2}\kappa_-\cos\left(\frac{\pi}{2}\kappa_+\right)\sin\left(\frac{\pi}{2}\kappa_-\right) = 0, \tag{30}$$

or

$$\mathcal{F}^-(\kappa_+, \kappa_-) := \frac{\pi}{2}\kappa_+\cos\left(\frac{\pi}{2}\kappa_+\right)\sin\left(\frac{\pi}{2}\kappa_-\right)$$
$$- \frac{\pi}{2}\kappa_-\sin\left(\frac{\pi}{2}\kappa_+\right)\cos\left(\frac{\pi}{2}\kappa_-\right) = 0. \tag{31}$$

on the wavenumbers κ_+ and κ_- must hold. Apart from a countable set of values of κ_+ and κ_-,

$$\mathcal{I}_1 = \{(\kappa_+, \kappa_-) : \kappa_+ = n + 2, \kappa_- = n, n \in \mathbb{N}\}, \tag{32}$$

where both (30) and (31) hold and the rank of the coefficient matrix of the system of boundary conditions is 2, in all other instances just one of (30) and (31) at a time is verified and the general solution has one undetermined constant, i.e. the rank of the coefficient matrix is 3. In that case, two possibilities are given.

When only (30) is satisfied, the non-trivial solution,

$$y(x_2) = 2L_2\hat{C}\left(\beta\sin\left(\kappa_-\frac{\pi x_2}{2L_2}\right) + \sin\left(\kappa_+\frac{\pi x_2}{2L_2}\right)\right) \tag{33}$$

with

$$\beta = -\frac{\kappa_+\cos\left(\frac{\pi}{2}\kappa_+\right)}{\kappa_-\cos\left(\frac{\pi}{2}\kappa_-\right)} \quad \text{or}$$
$$\beta = -\frac{\kappa_+^2\sin\left(\frac{\pi}{2}\kappa_+\right)}{\kappa_-^2\sin\left(\frac{\pi}{2}\kappa_-\right)} \quad \text{when } \kappa_- \text{ is an odd integer} \tag{34}$$

of the boundary-value problem (26) and (27) is odd in x_2 and can be shown to possess an even number of wrinkles. In passing, as there is some latitude in the definition, in the work of Puntel et al. (2011) and in the present work, the number of wrinkles is defined as the number of points along the line $x_1 = 0$ in which the slope of y is zero, that is where $y_{,2} = 0$.

When only (31) is satisfied, the solution,

$$y(x_2) = 2L_2\hat{D}\left(\alpha\cos\left(\kappa_-\frac{\pi x_2}{2L_2}\right) + \cos\left(\kappa_+\frac{\pi x_2}{2L_2}\right)\right) \tag{35}$$

with

$$\alpha = -\frac{\kappa_+\sin\left(\frac{\pi}{2}\kappa_+\right)}{\kappa_-\sin\left(\frac{\pi}{2}\kappa_-\right)} \quad \text{or}$$
$$\alpha = -\frac{\kappa_+^2\cos\left(\frac{\pi}{2}\kappa_+\right)}{\kappa_-^2\cos\left(\frac{\pi}{2}\kappa_-\right)} \quad \text{when } \kappa_- \text{ is an even integer}, \tag{36}$$

of (26) and (27) is even in x_2 and possesses an odd number of wrinkles.

Puntel et al. (2011) show that the first buckling mode observed in the sheet alternatively coincides with solution (33) or (35) according to the value of κ_+ (or κ_-), which, in turn, is related to the amount of applied stretch ε. When the floor of κ_+, denoted by $\lfloor\kappa_+\rfloor$ and defined as

$$\lfloor\kappa_+\rfloor = \max\{m \in \mathbb{N}, m \leqslant \kappa_+\} \tag{37}$$

is even, the solution coincides with (33). Otherwise, when $\lfloor\kappa_+\rfloor$ is odd, the solution coincides with (35). In any case, the number of wrinkles is equal to $\lfloor\kappa_+\rfloor$. Analytical plots of wrinkle profiles at $x_1 = 0$ for different values of κ_+ are shown in Fig. 1. In addition to providing visual confirmation concerning the parity of $y = w(0, \cdot)$ and the number of wrinkles, Fig. 1 shows that the wrinkle amplitude is not constant and that wrinkles are instead contained in a semi-sinusoidal envelope of wavelength $4L_2$. The amplitude is maximum at $x_2 = 0$ and decreases towards the free edges.

Based on the aforementioned observations, whenever κ_+ reaches an integer value a new wrinkle is formed and the character of the solution changes abruptly. These values of κ_+ coincide with the values of set $\mathcal{I}_1$ in (32) and determine a corresponding sequence of critical stretches ε. For each n in (32) such that $\kappa_- = \kappa_+ - 2 = n$, Puntel et al. (2011) show that the value of the relative applied stretch defined in (28) equals

$$e_n = r^2(\kappa_+^2 + \kappa_-^2 + r^2\kappa_+^2\kappa_-^2) = r^2((n+2)^2(1 + r^2n^2) + n^2), \tag{38}$$
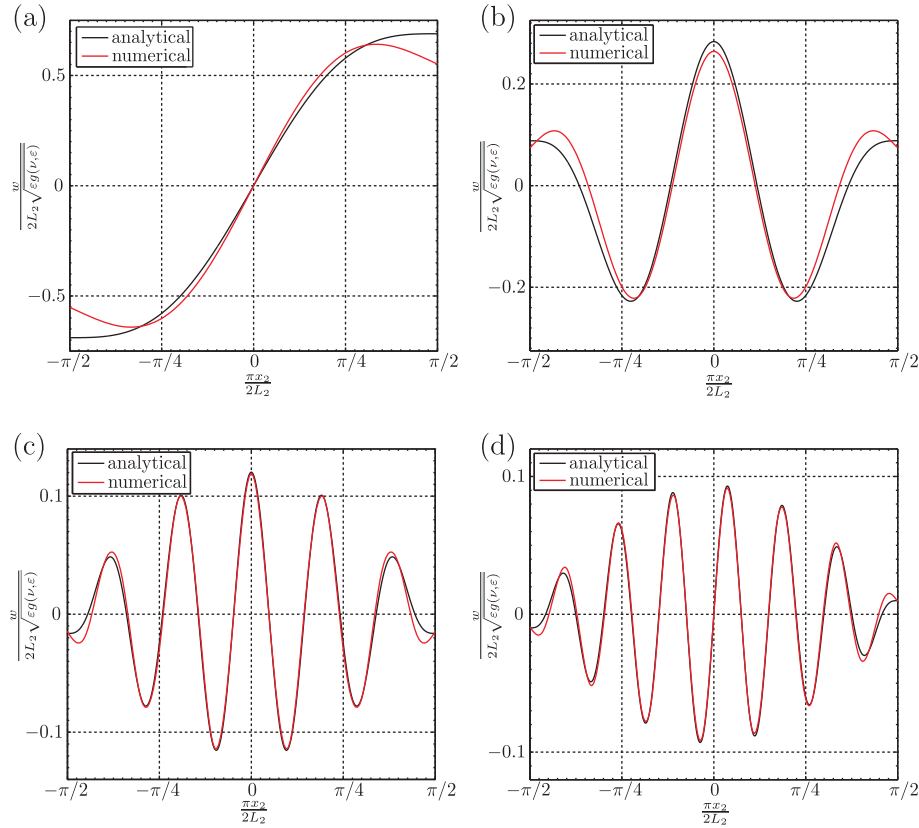
where the aspect ratio

Fig. 1. Plots of wrinkle profiles (a) $\kappa_+ = 2.5$, $\kappa_- = 0.8$, and $\beta = 7.21$; (b) $\kappa_+ = 5.5$, $\kappa_- = 3.63$, and $\alpha = 1.95$; (c) $\kappa_+ = 11.5$, $\kappa_- = 9.56$, and $\alpha = 1.33$; (d) $\kappa_+ = 14.5$, $\kappa_- = 12.5$, and $\beta = 1.25$.

$$r = \frac{L_1}{L_2} \tag{39}$$

has been introduced. Using the definitions of e and $\bar{\varepsilon}$ in (28) and of r above, a critical value of the applied stretch

$$\varepsilon_n = \frac{\pi^2 h^2}{48(1 - v^2)L_1^2}\left[1 + \frac{L_1^2}{L_2^2}\left((n+2)^2\left(1 + \frac{L_1^2 n^2}{L_2^2}\right) + n^2\right)\right] \tag{40}$$

corresponding to the onset of $n + 2$ wrinkles is obtained. For $\varepsilon_n \leqslant -\varepsilon < \varepsilon_{n+1}$, the sheet possesses $n + 2$ wrinkles.

In addition to the characterization of the critical stretches associated with solutions having a given number of wrinkles, the two other main analytical results of the work of Puntel et al. (2011) concern the determination of wrinkle amplitude and wavelength. The expressions for y in (33) and (35) depend, respectively, on undetermined constants $\hat{C}$ and $\hat{D}$. On substituting (33) and (35) into the Ansatz (23) and then into the linearized constraint (17), it becomes possible to compute in closed form the value of $\hat{C}$ or $\hat{D}$ such that the area of the deformed surface of the sheet attains the prescribed value. As a result, the wrinkle amplitude, conventionally computed at $x_1 = 0$, is obtained. Since wrinkles do not have all the same amplitude in the x_2-direction either, two measures are introduced: the maximum amplitude and the root-mean-square amplitude, that is the root-mean-square of the deflection of the points whose slope in direction x_2 is zero. Plots of the analytical results for the inverse of the root-mean-square amplitude and the inverse of the maximum amplitude versus the quartic root of the relative applied stretch e divided by the aspect ratio r are provided in Fig. 3. The evident jumps in the plots coincide with values (38) of e at which a new wrinkle is formed. An underlying linear trend,

$$A_{\text{rms}} \approx \sqrt{g(v, \varepsilon)}\sqrt[4]{\frac{64 h^2 L_1^2 \varepsilon}{3\pi^2(1 - v^2)}} \tag{41}$$

shown by a thin gray line, is easily revealed. Remarkably, plots for different aspect ratios r in Puntel et al. (2011) exhibit no appreciable difference but for very low values of the relative applied stretch e.

As for the wavelength, a rearrangement of (29) yields

$$\frac{y(x_2)}{2L_2} = \left[(\hat{A} + \hat{D})\cos\left(\frac{\kappa_+ + \kappa_-}{2}\frac{\pi x_2}{2L_2}\right) + (\hat{B} + \hat{C})\sin\left(\frac{\kappa_+ + \kappa_-}{2}\frac{\pi x_2}{2L_2}\right)\right]$$
$$\times \cos\left(\frac{\kappa_+ - \kappa_-}{2}\frac{\pi x_2}{2L_2}\right) + \left[(\hat{C} - \hat{B})\cos\left(\frac{\kappa_+ + \kappa_-}{2}\frac{\pi x_2}{2L_2}\right)\right.$$
$$\left. + (\hat{A} - \hat{D})\sin\left(\frac{\kappa_+ + \kappa_-}{2}\frac{\pi x_2}{2L_2}\right)\right]\sin\left(\frac{\kappa_+ - \kappa_-}{2}\frac{\pi x_2}{2L_2}\right) \tag{42}$$

from which it is easily deduced that the wrinkle wavelength is given by

$$\lambda = \frac{8L_2}{\kappa_+ + \kappa_-}. \tag{43}$$

A plot of the inverse of the analytical expression of λ in (43) versus the quartic root of the relative applied stretch e divided by the aspect ratio r is given in Fig. 4. The linear trend

$$\lambda \approx \sqrt[4]{\frac{16\pi^2 h^2 L_1^2}{3(1 - v^2)\varepsilon}} \tag{44}$$

is even more marked than in the amplitude plots in Fig. 3 and again low sensitivity for different aspect ratios r except for low values of e was observed by Puntel et al. (2011).

4. Assessment on the role of the geometric constraint

The crucial and unusual role played by the geometric constraint (9) in the variational formulation adopted in this work deserves further consideration and discussion.

The membranal stress state in a thin sheet in tension clamped at opposite ends is studied numerically in Fischer et al. (2000), who show that the in-plane stress state is inhomogeneous and entails zones of transversal compressive stresses close, but not adjacent, to the clamped ends. On the other hand this work, Puntel et al. (2011), and Cerda and Mahadevan (2003) before them, adopt a tensile homogeneous membranal stress state for which there can be no buckling independently of the amount of applied stretch. As emphasized in the Introduction, the geometric constraint is precisely a measure that forces an otherwise stable system to explore wrinkled configurations.

This constraint has been introduced due to the lack of an analytical solution for the pre-buckling inhomogeneous stress state. It is worth mentioning that the geometric constraint is not a means to circumvent the complex coupling between out-of-plane and in-plane displacements which is in the present treatment accounted for by the Föppl–von Kármán formulation.

Two possible motivations for the geometric constraint can be provided:

– In the wrinkled configuration, the transversal compressive stresses vanish; therefore the actual in-plane stress state resembles more closely an uniaxial stress state in the wrinkled configuration (the final state we are interested in) than it does in the pre-buckled configuration.
– Even if it is not explicitly quantified in the present work, it is reasonable to expect a variation of the area of the specimen when wrinkling occurs.

Though one may not necessarily like this constraint, to our knowledge there is hardly any alternative analytical approach to the wrinkling of a thin sheet in tension. By employing the constraint in Puntel et al. (2011), several results were obtained. Moreover, it was possible to predict, without prescribing them, wrinkled configurations with decaying amplitude towards the free edges while, always to our knowledge, practically all studies dedicated to the quantification of wrinkling assume wrinkles with constant amplitude or anyway assume the wrinkle shape a priori. Experimental results in Cerda et al. (2002) and Zheng (2009) and numerical results in Friedl et al. (2000), Nayyar et al. (2011) and Zheng (2009) confirm that the wrinkle amplitude is not constant and decays from the mid-line to the free edges of the sheet.

Finally let us motivate why, in prescribing the geometrical constraint in Eq. (9), we have not specified explicitly the amount of the area variation and instead we have stated that it depends on an unassigned function g of the applied stretch ε and of Poisson's ratio ν. There are at least two reasons for this choice:

– To establish a scaling relationship for the amplitude and to discuss several other properties concerning wrinkle amplitude, it is not necessary to prescribe an explicit value for g.
– Different studies have different values for g. In Cerda and Mahadevan (2003), $g = \nu$. In Wong and Pellegrino (2006b) where the wrinkling of an in-plane sheared sheet is studied, the same scaling relationship holds but with $g(\nu, \varepsilon) = (1 - \nu)/2$. The comparison holds under the provision that the length of the wrinkles and the maximum principal stress are aptly translated to that different setting. Finally, for the same problem of wrinkling under in-plane shear, Epstein (2003) finds $g = (3\pi/4\sqrt{2}) \cdot (1 - \nu)/2$. For $\nu = 1/3$, we have $\nu = (1 - \nu)/2 = 1/3$ so that the values of g found in Cerda and Mahadevan (2003) and Wong and Pellegrino (2006b) coincide. Curiously, in the experiments of Cerda et al. (2002) and of Wong and Pellegrino (2006a), the value of ν are near 1/3, 0.35 for Cerda, Ravi Chandar and Mahadevan and 0.31 for Wong and Pellegrino.

5. Variational formulation

It is straightforward to derive variational forms of the Euler–Lagrange Eqs. (10) and (19) with the boundary conditions (11), (12) and (20), (21) because they follow from the first variation of the energy functionals (6) and (18), respectively.

An arbitrary virtual deflection field v is referred to as kinematically admissible if

$$v = 0 \quad \text{and} \quad v_{,n} = 0 \quad \text{on } \partial\Omega_{\text{fxd}}. \tag{45}$$

$\mathcal{W}$ and $\mathcal{L}$ are the spaces of admissible deflection and Lagrange multiplier fields, respectively. The variational form reads: find (w, ε^*) belonging to $\mathcal{W} \times \mathcal{L}$ such that[2]

$$T(w, \varepsilon^*, v, \eta^*) = 0 \tag{46}$$

for all (v, η^*) belonging to $\mathcal{W} \times \mathcal{L}$, where

$$T(w, \varepsilon^*, v, \eta^*) = \int_\Omega \Big(Bw_{,\alpha\alpha}v_{,\beta\beta} - B(1-\nu)(w_{,\alpha\alpha}v_{,\beta\beta} - w_{,\alpha\beta}v_{,\alpha\beta})$$
$$+ \frac{Eh}{2b}(w_{,\alpha}w_{,\alpha})(w_{,\beta}v_{,\beta}) + Eh\varepsilon w_{,1}v_{,1}$$
$$- Eh\varepsilon^* \frac{w_{,\alpha}v_{,\alpha}}{\sqrt{1 + w_{,\beta}w_{,\beta}}}\Big) da - \eta^* \mathcal{T}. \tag{47}$$

When linearized in accord with the small-slope approximation (15), T in (47) is replaced by

$$T_{\text{lin}}(w, \varepsilon^*, v, \eta^*) = \int_\Omega \Big(Bw_{,\alpha\alpha}v_{,\beta\beta} - B(1-\nu)(w_{,\alpha\alpha}v_{,\beta\beta} - w_{,\alpha\beta}v_{,\alpha\beta})$$
$$+ Eh\varepsilon w_{,1}v_{,1} - Eh\varepsilon^* w_{,\alpha}v_{,\alpha}) da - \eta^* \mathcal{T}_{\text{lin}} \tag{48}$$

and the variational formulation reads: find (w, ε^*) belonging to $\mathcal{W} \times \mathcal{L}$ such that

$$T_{\text{lin}}(w, \varepsilon^*, v, \eta^*) = 0 \tag{49}$$

for all (v, η^*) belonging to $\mathcal{W} \times \mathcal{L}$. It is important to remark that T_{lin} is not linear because the term $\mathcal{T}_{\text{lin}}$ defined in Eq. (17) is quadratic in the gradient of w.

6. Finite-element discretization with B-splines

The Euler–Lagrange equation (10) arising from the net-potential energy (6) involves fourth-order partial derivatives. Hence, a standard Galerkin approximation requires C^1-continuous basis functions with continuity of the deflection field and of its first derivatives. In the present study, we use bicubic B-splines that are globally C^2-continuous and thus satisfy the requirement of the solution space for fourth-order problems.

The space of admissible deflection fields is a subset $\mathcal{W}$ of $H^2(\Omega)$, where $H^m(\Omega)$ denotes the Sobolev space of order m. We use a standard Galerkin method using B-splines to approximate the solution to (46) and state the weak form of the variational problem in terms of the finite-element space $\mathcal{W}^h$ contained in $H^2(\Omega)$. Here, the Lagrange multiplier ε^* and its corresponding test value η^* are scalars. In addition, to construct the basis functions of $\mathcal{W}^h$, a regular finite-element partition is considered, namely $\Omega^h = \cup_{e=1}^M \Omega_e$, with $\Omega^h \approx \Omega$ and M the total number of elements in the mesh.

The finite-element formulation proposed to approximate the solution to the nonlinear governing Eq. (10) can then be stated as: find (w^h, ε^*) belonging to $\mathcal{W}^h \times \mathcal{L}$ such that

$$T(w^h, \varepsilon^*, v^h, \eta^*) = 0 \tag{50}$$

---

[2] Since the natural boundary conditions in our case are homogeneous, we can set the right hand-side of (46) and (49) to zero.

for all (v^h, η^*) belonging to $\mathcal{W} \times \mathcal{L}$. The left-hand side is defined by substituting w^h and v^h into (47) and integrating over Ω^h. When considering the linear governing equation (19) instead of (10), T in (50) is replaced by T_{lin}.

The formulation based on bicubic B-splines employs a uniform set of grid points I. The approximation to the deflection field is then given by

$$w^h(\mathbf{x}) = \sum_I N_I(\mathbf{x}(\xi))\hat{w}_I = \mathbf{N} \cdot \hat{\mathbf{w}}, \tag{51}$$

where $\hat{w}_I$ is the nodal value at node I. Here, N_I is the I-th B-spline basis function and ξ denotes the parametric coordinates used to construct the B-spline basis. Accordingly, $\mathbf{N}$ and $\hat{\mathbf{w}}$ are the vectors of nodal shape functions and nodal values, respectively. The corresponding virtual deflection field v can be approximated in the same way.

A brief account of the B-spline basis functions in one dimension is given below. Extension to multiple dimensions is straightforward with the use of tensor product splines. A more detailed treatment of the subject is provided by Piegl and Tiller (1997).

Consider a knot vector Ξ, where

$$\Xi = \{\xi_1, \xi_2, \ldots, \xi_{n+p+1}\}, \tag{52}$$

with n denoting the number of knots and p the degree of the spline. B-spline basis functions are defined recursively starting with piecewise constants (degree $p = 0$):

$$N_{I,0}(\xi) = \begin{cases} 1 & \text{if } \xi_I \leqslant \xi < \xi_{I+1}, \\ 0 & \text{otherwise}. \end{cases} \tag{53}$$

For $p \geqslant 1$,

$$N_{I,p}(\xi) = \frac{\xi - \xi_I}{\xi_{I+p} - \xi_I} N_{I,p-1}(\xi) + \frac{\xi_{I+p+1} - \xi}{\xi_{I+p+1} - \xi_{I+1}} N_{I+1,p-1}(\xi). \tag{54}$$

7. Algorithmic linearization of the variational form

The variational forms (46) and (49) are nonlinear. A full Newton–Raphson iteration scheme is used here to resolve the nonlinear system of equations. The derivation of the consistent tangent stiffness matrix to be employed in the full Newton–Raphson strategy is provided below.

For convenience, we use the notation

$$(w, v)_\Omega = \int_\Omega wv \, da.$$

The variational formulation (46) can be restated as a nonlinear finite-element problem in terms of a residual R as

$$R(w, \varepsilon^*, v, \eta^*) = R_w(w, \varepsilon^*, v) + R_{\varepsilon^*}(w, \eta^*) = 0, \quad \forall v \in \mathcal{W}, \ \forall \eta^* \in \mathcal{L}. \tag{55}$$

In (55), $R_w(w, \varepsilon^*, v)$ and $R_{\varepsilon^*}(w, \eta^*)$ correspond to the first and second addend on the right-hand side of (47) where $T(w, \varepsilon^*, v, \eta^*)$ is defined. In the case of small-slope approximation two terms $R_w(w, \varepsilon^*, v)$ and $R_{\varepsilon^*}(w, \eta^*)$ are analogously obtained from the first and second addend on the right-hand side of Eq. (48) where $T_{\text{lin}}(w, \varepsilon^*, v, \eta^*)$ is defined. Equivalently, (55) can be rewritten as

$$R_w(w, \varepsilon^*, v) = 0, \quad \forall v \in \mathcal{W} \quad \text{and} \quad R_{\varepsilon^*}(w, \eta^*) = 0, \quad \forall \eta^* \in \mathcal{L}. \tag{56}$$

For given solutions w_n and ε_n^* at the n-th iteration, (55) is linearized as

$$0 = R(w_{n+1}, \varepsilon_{n+1}^*, v, \eta^*) \simeq R(w_n, \varepsilon_n^*, v, \eta^*) + \left.\frac{\partial R}{\partial w}\right|_n dw + \left.\frac{\partial R}{\partial \varepsilon^*}\right|_n d\varepsilon^*,$$
$$\forall v \in \mathcal{W}, \ \forall \eta^* \in \mathcal{L}, \tag{57}$$

or, alternatively,

$$0 = R_w(w_{n+1}, \varepsilon_{n+1}^*, v) \simeq R_w(w_n, \varepsilon_n^*, v) + \left.\frac{\partial R_w}{\partial w}\right|_n dw + \left.\frac{\partial R_w}{\partial \varepsilon^*}\right|_n d\varepsilon^*,$$
$$\forall v \in \mathcal{W} \tag{58}$$

and

$$0 = R_{\varepsilon^*}(w_{n+1}, \eta^*) \simeq R_{\varepsilon^*}(w_n, \eta^*) + \left.\frac{\partial R_{\varepsilon^*}}{\partial w}\right|_n dw, \quad \forall \eta^* \in \mathcal{L} \tag{59}$$

for increments dw and $d\varepsilon^*$ of the deflection w and the Lagrange multiplier ε^*, respectively.

The increments found in (57) or in (58) and (59) are used to update the solution:

$$w_{n+1} = w_n + dw = \mathbf{N} \cdot (\hat{\mathbf{w}}_n + d\hat{\mathbf{w}}) \quad \text{and} \quad \varepsilon_{n+1}^* = \varepsilon_n^* + d\varepsilon^*. \tag{60}$$

The increments of R are obtained as

$$\frac{\partial R}{\partial w} dw = \frac{\partial R_w}{\partial w} dw + \frac{\partial R_{\varepsilon^*}}{\partial w} dw \quad \text{and} \quad \frac{\partial R}{\partial \varepsilon^*} d\varepsilon^* = \frac{\partial R_w}{\partial \varepsilon^*} d\varepsilon^*, \tag{61}$$

where

$$\frac{\partial R_w}{\partial w} dw = Bv(dw_{,\alpha\alpha}, v_{,\alpha\alpha})_\Omega + B(1-v)(dw_{,\alpha\beta}, v_{,\alpha\beta})_\Omega + Eh\varepsilon(dw_{,1}, v_{,1})_\Omega$$
$$+ \frac{Eh}{b}((w_{,\alpha}w_{,\beta})dw_{,\beta}, v_{,\alpha})_\Omega + \frac{Eh}{2b}((w_{,\beta}w_{,\beta})dw_{,\alpha}, v_{,\alpha})_\Omega$$
$$- Eh\varepsilon^*\left(\frac{dw_{,\alpha}}{\sqrt{1+w_{,\beta}w_{,\beta}}}, v_{,\alpha}\right)_\Omega + Eh\varepsilon^*\left(\frac{(w_{,\alpha}w_{,\beta})dw_{,\beta}}{(1+w_{,\gamma}w_{,\gamma})^{\frac{3}{2}}}, v_{,\alpha}\right)_\Omega, \tag{62}$$

$$\frac{\partial R_w}{\partial \varepsilon^*} d\varepsilon^* = -Ehd\varepsilon^*\left(\frac{w_{,\alpha}}{\sqrt{1+w_{,\beta}w_{,\beta}}}, v_{,\alpha}\right)_\Omega, \tag{63}$$

and

$$\frac{\partial R_{\varepsilon^*}}{\partial w} dw = -Eh\eta^*\left(\frac{dw_{,\alpha}}{\sqrt{1+w_{,\beta}w_{,\beta}}}, w_{,\alpha}\right)_\Omega. \tag{64}$$

When the small-slope approximation (15) is enforced, Eqs. (62)–(64) simplify to

$$\frac{\partial R_w}{\partial w} dw = Bv(dw_{,\alpha\alpha}, v_{,\alpha\alpha})_\Omega + B(1-v)(dw_{,\alpha\beta}, v_{,\alpha\beta})_\Omega$$
$$+ Eh\varepsilon(dw_{,1}, v_{,1})_\Omega - Eh\varepsilon^*(dw_{,\alpha}, v_{,\alpha})_\Omega, \tag{65}$$

$$\frac{\partial R_w}{\partial \varepsilon^*} d\varepsilon^* = -Ehd\varepsilon^*(w_{,\alpha}, v_{,\alpha})_\Omega, \tag{66}$$

and

$$\frac{\partial R_{\varepsilon^*}}{\partial w} dw = -Eh\eta^*(dw_{,\alpha}, w_{,\alpha})_\Omega. \tag{67}$$

On considering the finite-element approximation introduced in (51) and substituting (62)–(64) or (65)–(67) into (58) and (59), a linear system of equations,

$$\mathbf{Kd} = -\mathbf{R} \tag{68}$$

is obtained, where the tangent stiffness matrix $\mathbf{K}$ and the residual vector $\mathbf{R}$ are defined as

$$\mathbf{K} = \begin{bmatrix} \mathbf{K}_{ww} & \mathbf{K}_{w\varepsilon^*} \\ \mathbf{K}_{\varepsilon^*w} & 0 \end{bmatrix} \tag{69}$$

and

$$\mathbf{R} = \begin{bmatrix} \hat{\mathbf{R}}_w(\hat{\mathbf{w}}_n, \varepsilon_n^*) \\ R_{\varepsilon^*}(\hat{\mathbf{w}}_n) \end{bmatrix}. \tag{70}$$

Here, $\mathbf{d} = (d\hat{\mathbf{w}}, d\varepsilon^*)^\top$ represents the increment of the deflection w and the Lagrange multiplier ε^*. We obtain the increments $d\hat{\mathbf{w}}$ and

$d\varepsilon^*$ using (68) and then update the solution using (60) until it is convergent. The matrices $\mathbf{K}_{ww}$, $\mathbf{K}_{w\varepsilon^*}$ and $\mathbf{K}_{\varepsilon^*w} = \mathbf{K}_{w\varepsilon^*}^\top$ originate from (62)–(64) for the nonlinear case and (65)–(67) for the linear case. The residual vectors $\hat{\mathbf{R}}_w$ and R_{ε^*} stem from R_w and R_{ε^*} in (55), respectively.

8. Numerical studies

In the following we assign a value of the applied stretch and seek the stationarity point of potential energy functionals (6) and (18) subject to the geometric constraint (9) and (17), respectively. As we already noted, since the prescribed area of the sheet is slightly larger than the area of the flat reference configuration, the system is forced to adopt a wrinkled configuration. We neither discuss the local stability of the solution nor follow bifurcated paths in the fashion of a post-buckling analysis.

Initially, the small-slope approximation (15) is adopted and thus the linearized variational formulation (49) is considered. Comparison with the results of Puntel et al. (2011) allows assessment of the influence on the results of the Ansatz (23) and of the simplified boundary conditions (24) and (25). Later, the nonlinear case (46) will be briefly studied allowing an appraisal of the role of the small-slope approximation. Unless otherwise indicated, all simulations are performed at a grid resolution of 30^2.

We consider a rectangular sheet of length $L_1 = 10$ cm, width $L_2 = 6$ cm, and thickness $h = 0.01$ cm, with Young's modulus $E = 1$ GPa and Poisson's ratio $\nu = 0.35$, gripped on the edges $x_1 = \pm L_1$ and subject to a stretch ε. Motivated by experiments of Cerda et al. (2002), we consider boundary conditions with traction-free conditions (21) at free edges $\partial\Omega_\text{free}$ and fixed conditions (20) at clamped edges $\partial\Omega_\text{fxd}$. Since B-splines are non-interpolatory basis functions, we use a standard penalty approach with the penalty parameter $\tau = 10^8$ to weakly impose Dirichlet boundary conditions (20) at clamped edges (see, for example, Embar et al. (2010)). Consistent with the boundary conditions (20) on the pinned ends of the sheet, we take the initial guess

$$w(x_1, x_2) = \left(\frac{x_1^2}{L_1^2} - 1 \right)^2 y(x_2) \tag{71}$$

for the Newton–Raphson iteration method. Here, y is defined via (33) or (35).

In Fig. 1, to verify our algorithm, we first begin by comparing wrinkle profiles with those obtained from analytical solutions of (26). Plots are provided for results obtained using four cases of initial guesses with the parameter values: (a) $\kappa_+ = 2.5$, $\kappa_- = 0.8$, and $\beta = 7.21$; (b) $\kappa_+ = 5.5$, $\kappa_- = 3.63$, and $\alpha = 1.95$; (c) $\kappa_+ = 11.5$, $\kappa_- = 9.56$, and $\alpha = 1.33$; (d) $\kappa_+ = 14.5$, $\kappa_- = 12.5$, and $\beta = 1.25$. All

wrinkled solutions are hardly distinguishable from analytical solutions and have peaks at $x_2 = 0$. A slight discrepancy between the solutions is found at both ends because traction-free conditions have a localized influence at the free-edges. Significantly, the main findings of Puntel et al. (2011) are confirmed, in that as the wavenumber κ_+ increases, the number of wrinkles grows accordingly, and wrinkles are enclosed in semi-sinusoidal envelopes with wavelength approaching $4 L_2$. As a result, the wrinkle amplitude is maximized at the mid-line $x_2 = 0$ and is close to 0 at the free edges $x_2 = \pm L_2$. Different solutions are obtained by choosing different values of the wavenumber κ_+ in the initial guess, e.g., for $x_2 = 0$, (a) and (d) are odd and (b) and (c) are even.

Fig. 2 shows the surface plot of the deflection w obtained using an initial guess with the parameter values $\kappa_+ = 8.5$, $\kappa_- = 6.58$, and $\varepsilon = 5.7 \times 10^{-3}$. We also display the wrinkle profile along the line $x_2 = 0$. The surface plot clearly shows the sinusoidal envelope enclosing the wrinkles with wavelength 2π and the wrinkles decaying toward the free edges. These characteristics of wrinkled solutions are consistent with analytical results of Puntel et al. (2011).

Fig. 3a shows the inverse $1/A_\text{rms}$ of the root-mean-square amplitude, multiplied by $L_2\sqrt{2\varepsilon g(\nu, \varepsilon)}$, versus $e^{1/4}/r$. The numerical root-mean-square wrinkle amplitude is obtained by considering the wrinkle amplitude of all local maxima and minima of the wrinkle profile at $x_1 = 0$ and computing their root-mean-square average. The plot shows that the numerical results are very close to the analytical solutions, especially at high values of the abscissa. Importantly, both numerical and analytical results show a linear trend with a slope of $\pi/4$ represented by a thin black line. We note that this line coincides with the scaling relation for the amplitude obtained by Cerda and Mahadevan (2003) for provided that $g(\nu, \varepsilon) = \nu$. As mentioned in Section 3, the jumps in the plot correspond to the points of solution set where the amplitude cannot be computed and the solution changes abruptly from symmetric about the line $x_2 = 0$ to antisymmetric or vice versa. In Fig. 3b, the inverse $1/A_\text{max}$ of the maximum amplitude, multiplied by $2L_2\sqrt{\varepsilon g(\nu, \varepsilon)}$, is plotted versus $e^{1/4}/r$. Again, numerical results are favorably comparable to the analytical results obtained from Puntel et al. (2011). The deviation from the linear trend, indicated by a thin black line, is even less significant than in Fig. 3a.

As far as the wavelength λ is concerned, Fig. 4 shows a plot of $1/\lambda$, multiplied by $2L_2$, versus $e^{1/4}/r$. Both numerical and analytical results exhibit the same linear trend with a slope of $1/2$. Moreover, this trend agrees with the scaling relation predicted by Cerda and Mahadevan (2003) and experimental measurements of Cerda et al. (2002). The numerical evaluation of the wavelength is performed by taking the double of the ratio between the distance separating the first and last wrinkle and the number of wrinkles
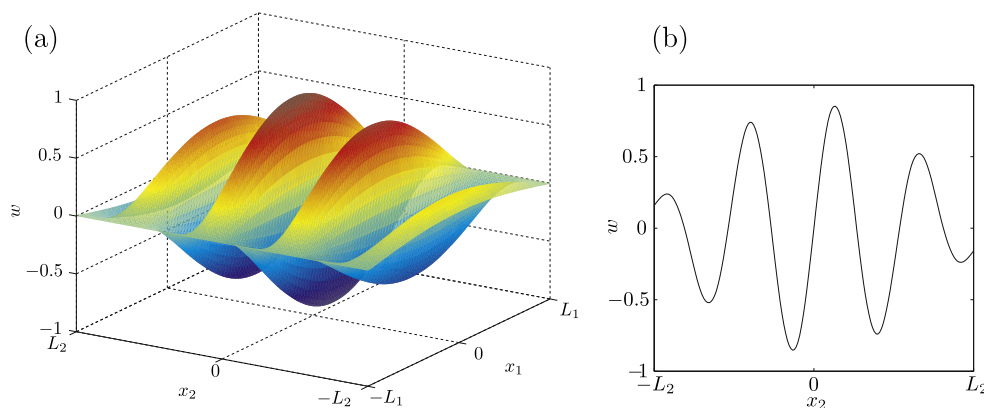

Fig. 2. (a) Surface plot and (b) wrinkle profile of the deflection field w for $\kappa_+ = 8.5$ and $\kappa_- = 6.58$ with the applied stretch $\varepsilon = 5.7 \times 10^{-3}$.
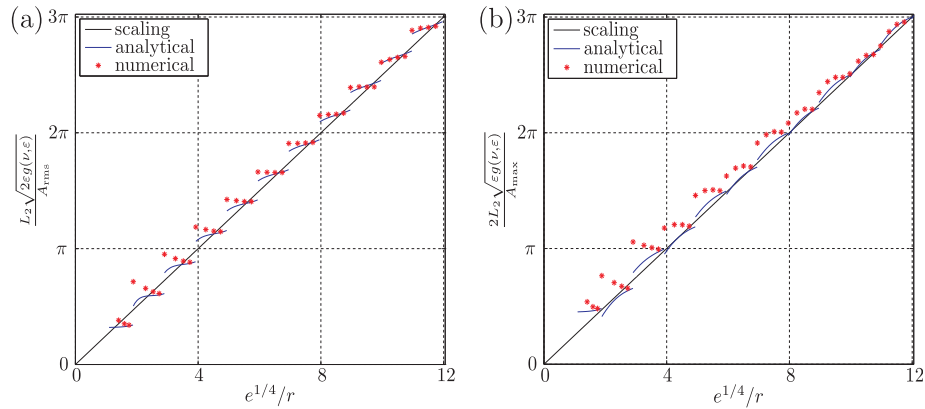
Fig. 3. (a) The inverse $L_2\sqrt{2\varepsilon g(v,\varepsilon)}/A_{\text{rms}}$ of the root-mean-square of the wrinkle amplitude (b) The inverse $2L_2\sqrt{\varepsilon g(v,\varepsilon)}/A_{\text{max}}$ of the maximum amplitude, plotted versus $e^{1/4}/r$.
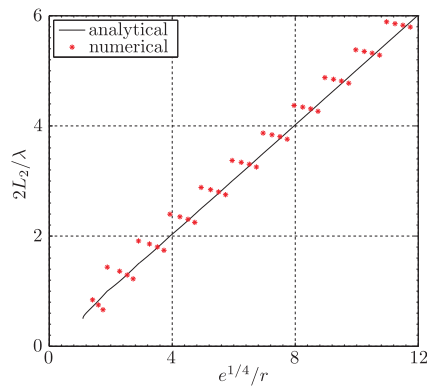

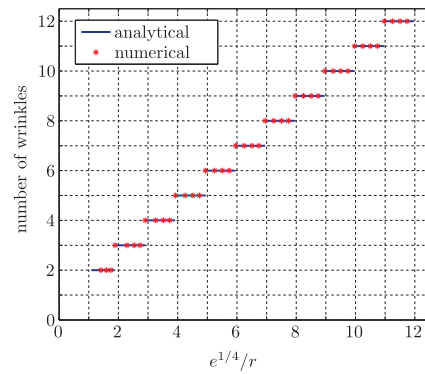**Fig. 4.** The inverse of wrinkle wavelength $2L_2/\lambda$ versus $e^{1/4}/r$.

Fig. 5. Plot of the number of wrinkles versus $e^{1/4}/r$.

decreased by one. When the number of wrinkles increases by one, the above computation has a jump which can be observed in Fig. 4.

In Fig. 5, we show the number of wrinkles plotted against $e^{1/4}/r$. Both numerical and analytical results are indistinguishable. Importantly, the results indicate that the number of wrinkles is proportional to $e^{1/4}/r$ and therefore, as expected, inversely proportional to the wavelength λ.

We now briefly study the nonlinear case that arises when the small-slope approximation (15) is not invoked. Hence, the variational form (46), (47) is considered to obtain wrinkled solutions. In this case, numerical computations were performed using the Newton–Raphson method combined with a line search algorithm (see, for example, Laursen (2002)) to obtain convergence results due to the high nonlinearity of the variational form. In Fig. 6, the wrinkle profiles of the nonlinear case are compared with those obtained from the variational form based on linearization. Plots are provided for results obtained using a grid resolution of 50^2 and initial guesses with the following parameter values: (a) $\kappa_+ = 5.5$, $\kappa_- = 3.63$, and $\alpha = 1.95$; (b) $\kappa_+ = 11.5$, $\kappa_- = 9.56$, and $\alpha = 1.33$. While the maximum amplitudes for the nonlinear cases are smaller than those of the linear cases and a little of discrepancy is found at both ends, they both have peaks at $x_2 = 0$ and show a sinusoidal envelope, with wavelength 2π, enveloping the wrinkles as the linear case does. comparable to those of the linearized ones.

Fig. 7 displays the inverse of the root-mean-square amplitude and wrinkle wavelength versus $e^{1/4}/r$ for the nonlinear case. Both results show the same linear trend with the linear case, i.e., a slope of $1/2$ for the wavelength and of $\pi/4$ for amplitude. These results indicate that, under linear-elastic assumptions and in the range of applied stretches considered, nonlinear effects associated with the small-slope approximation are not significant in the analysis of wrinkling of a stretched thin sheet.

9. Comparisons with experimental and numerical results

Next, comparisons with other experimental and numerical results available in the literature are provided.

9.1. Scaling laws

The scaling law for wrinkle wavelength in Eq. (44) and in Fig. 4 is experimentally confirmed by Cerda et al. (2002) and numerically by Nayyar et al. (2011).

As yet, experimental validation for the amplitude scaling law (41) has not been provided. Quite interestingly however, very similar scaling laws for both amplitude and wavelength are derived analytically by Wong and Pellegrino (2006b) for the case of a thin sheet subject to in-plane shear. The comparisons of the two scaling laws in Wong and Pellegrino (2006b) with the experiments performed by Wong and Pellegrino (2006a) are remarkably accurate.

The scaling law for the half wavelength

$$\frac{1}{2}\lambda_{WP} \approx \sqrt[4]{\frac{\pi^2 t^2 H^2}{3(1-v^2)\gamma}}$$

appearing in Wong and Pellegrino (2006b), matches identically the one presented in Eq. (44) provided that the length of the wrinkles and the maximum principal stress are aptly translated, namely by substituting $\gamma \to 2\varepsilon, H\sqrt{2} \to 2L_1$ and $t \to h$.
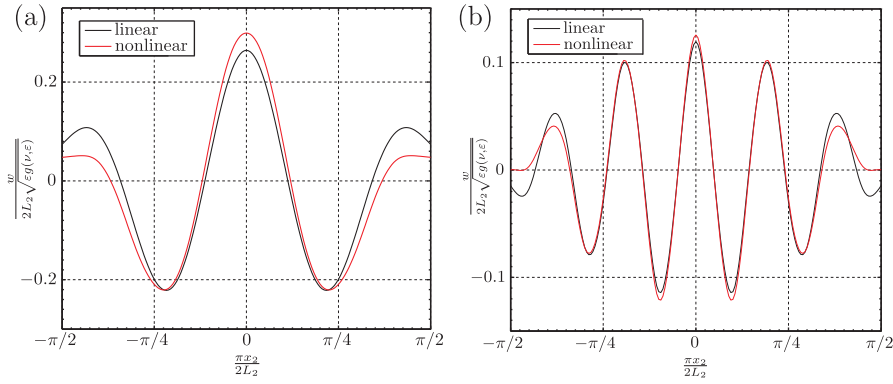
Fig. 6. Comparison of linear and nonlinear wrinkle shape profiles: (a) $\kappa_+ = 5.5$, $\kappa_- = 3.63$, and $\alpha = 1.95$; (b) $\kappa_+ = 11.5$, $\kappa_- = 9.56$, and $\alpha = 1.33$.
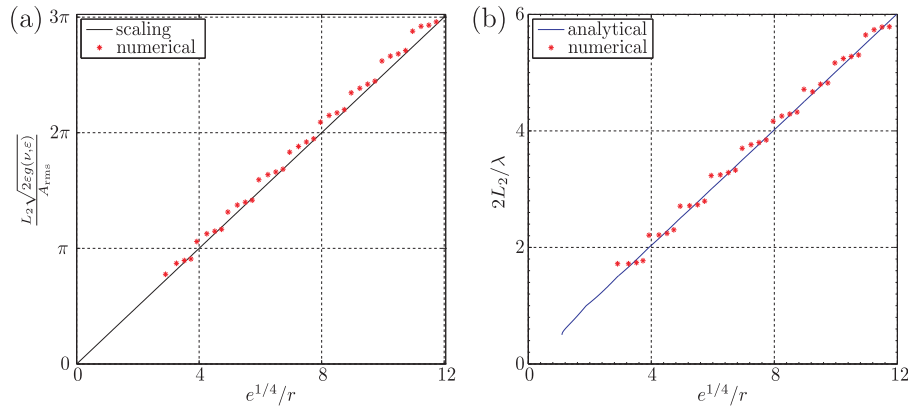

Fig. 7. (a) The inverse $L_2\sqrt{2\varepsilon g(v,\varepsilon)}/A_{\rm rms}$ of the root-mean-square of the wrinkle amplitude and (b) The inverse of wrinkle wavelength $2L_2/\lambda$, plotted versus $e^{1/4}/r$ for the nonlinear case.

With these same provisions and choosing $g(v,\varepsilon) = (1-v)/2$ in Eq. (41), also the scaling law of Wong and Pellegrino for the amplitude

$$A_{WP} \approx \sqrt[4]{\frac{4H^2 t^2 \gamma (1-v)^2}{3\pi^2(1-v^2)}}$$

is exactly recovered. There is therefore a noteworthy connection between the experimentally validated scaling law results presented in Wong and Pellegrino (2006b) and those presented herein.

9.2. Critical strains

We consider results that allow for an assessment of the validity of Eq. (40), relating geometric and material properties of the sheet to the stretch ε_n necessary to apply in order to induce $n + 2$ wrinkles.

We start by observing that, in Eq. (40), $\varepsilon_n \propto n^4$. Recall that we essentially count one wrinkle for each half wavelength of the sinusoidally shaped wrinkles. More precisely, the number of wrinkles is counted as the number of local minima and maxima of the out of plane displacement along a line parallel to the width of the sheet, having equation $x_1 = 0$.

For the aforementioned reasons, small miscalculations of the number of wrinkles can greatly change the corresponding value of the computed critical strain. In the case of wrinkles of vanishing amplitude towards the free edges it can be even more difficult to count wrinkles from a visual inspection of the numerical plot of a wrinkled sheet.

Setting aside the above disclaimer, we compared the critical strains provided by (40) to two numerical examples presented in the paper by Friedl et al. (2000).

By visual inspection of Figs. 7A and B in Friedl et al. (2000), we estimate 9 wrinkles, that is $n = 7$ in Eq. (40). In the first case $L_1 = 200$ mm, $L_2 = 100$ mm, $h = 0.05$ mm, $v = 0.3$ and Young's modulus $E = 70$ GPa. In the second case only the specimen length $L_1 = 700$ mm changes. The critical stress is 236 MPa in the first case and 761 MPa in the second. Multiplying ε_n in Eq. (40) of our paper by Young's modulus E and using $n = 7$ we obtain 63 MPa and 769 MPa respectively. Using $n = 9$ the former value increases from 63 MPa to 156 MPa. In one of the two examples we have a remarkably good correspondence, in the other we do not. There is here a first indication, confirmed in the next subsection, that the predictions of the present model are less accurate at low aspect ratios. However, as we said, $\varepsilon_n \propto n^4$ and it is difficult to precisely count wrinkles of vanishing amplitude.

Numerical and experimental results for wrinkling of stretched silicone rubber sheets can also be found in Zheng (2009). However we chose Friedl et al. (2000) over Zheng (2009) because the former uses a linear elastic material as we do, while the latter assumes a Mooney–Rivlin behavior. As for the experimental results, Zheng (2009) does not provide values of the critical strains. It turns out that the critical strains are very hard to measure experimentally. In the case of Zheng (2009), imperfections in sample preparation and mounting stages caused the specimens to wrinkle "immediately after the tensile load was applied" (see Zheng, 2009, pp. 53–54).

Another simple validation of the leading n^4 term in Eq. (40) can be indirectly obtained from the scaling law for wrinkle wavelength which, as we saw, is confirmed by numerical (Nayyar et al., 2011) and experimental (Cerda et al., 2002) evidence. Since roughly $\lambda \approx 4L_2/n$, see Eq. (43) with $\kappa_- = \kappa_+ - 2 = n$, and $\lambda \approx (4L_2 r)/e^{1/4}$, see Eq. (44), we obtain by elimination the leading term $e_n \propto r^4 n^4$ of Eqs. (38) and (40) of the present work.

9.3. Range of aspect ratios for which wrinkling does not occur

Zheng (2009) observes that, below a prescribed amount of applied strain, only sheets within a certain aspect ratio interval wrinkle. A contour map of the critical buckling strain for different sheet lengths and widths is shown in Fig. 8. Black dots in Fig. 8 indicate the actual simulations performed using a Mooney–Rivlin constitutive law. It can be seen that contour lines for strains higher than 0.4–0.6 are obtained by extrapolation. Zheng (2009) obtained a similar result in the experiments, summarized in Fig. 9. Black circles in Fig. 9 denote specimens that wrinkled at a strain lower than 1, i.e., 100%, while black crosses correspond to specimens that had not wrinkled at ε equal to 1. The dashed line is the trend line separating the wrinkled and non-wrinkled regions. There seems to be a discrepancy between numerical and experimental results since the experimental $\varepsilon = 1$ separation line overlaps the numerical $\varepsilon = 0.2$ contour line. In any case, both the experimental and numerical results in Zheng (2009) indicate that below a given applied strain, wrinkling is restricted to an interval of aspect ratios.

It is not easy, with the model proposed herein, to perform a direct comparison with Zheng's results. Our model does not provide the critical strain but a sequence ε_n of critical strains, each corresponding to a nontrivial configuration with $n + 2$ wrinkles.

We will attempt a comparison anyway by fixing the number of wrinkles and discussing how the critical strain ε_n changes with the dimensions of the sheet. We will see that the present work predicts an effect of the aspect ratio not so dissimilar from that observed by Zheng (2009).

By solving Eq. (40) of the present work for L_1, we find that wrinkled configurations with $n + 2$ wrinkles are possible below an assigned strain ε when

$$L_1 < \frac{L_2}{\sqrt{2k}}\sqrt{c^2 L_2^2 - p + \sqrt{\left(c^2 L_2^2 - p\right)^2 - 4k}} \qquad (72)$$

and

$$L_1 > \frac{L_2}{\sqrt{2k}}\sqrt{c^2 L_2^2 - p - \sqrt{\left(c^2 L_2^2 - p\right)^2 - 4k}}, \qquad (73)$$
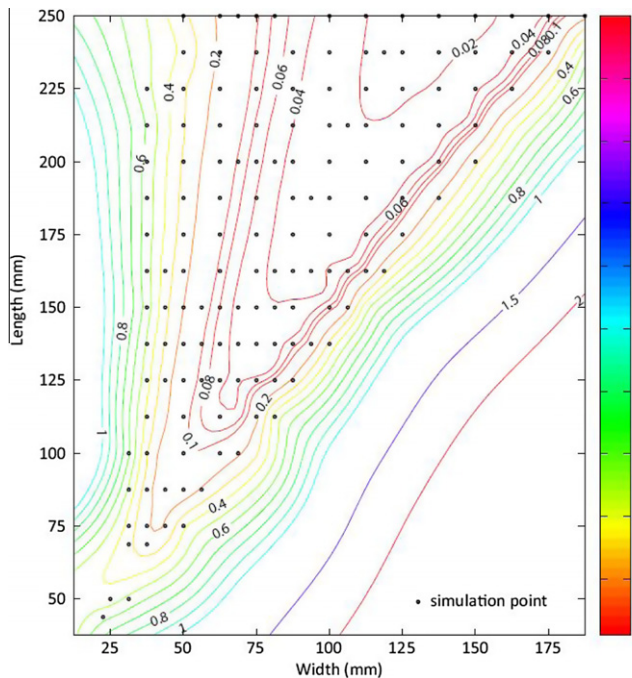

Fig. 8. Fig. 4.5 of Zheng's Ph.D. thesis (Zheng, 2009). Contour map of the computed critical buckling strain for 0.1 mm (0.004 in.) membranes.
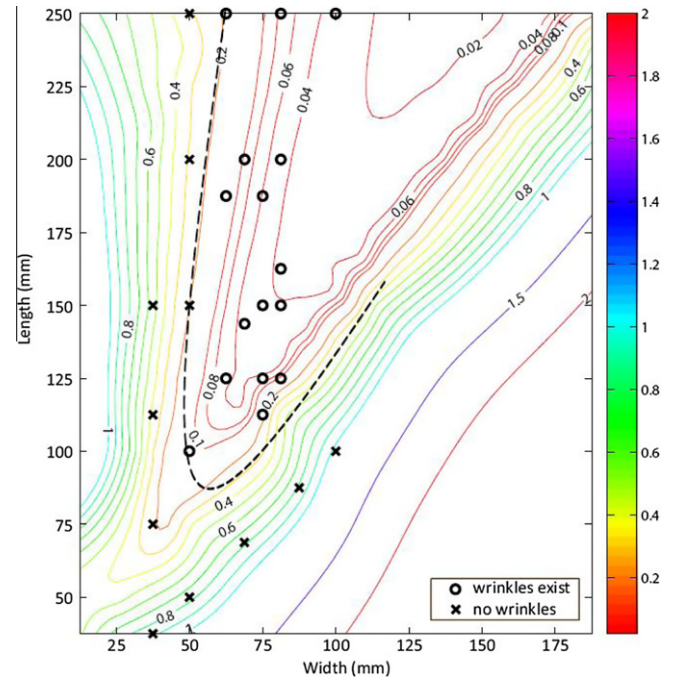

Fig. 9. Fig. 5.1 of Zheng's Ph.D. thesis (Zheng, 2009). Contour map of the computed critical buckling strain of various membrane dimensions overlapped with wrinkle existence map obtained from experiments. The dashed line is the trend line separating the wrinkled and non-wrinkled regions.
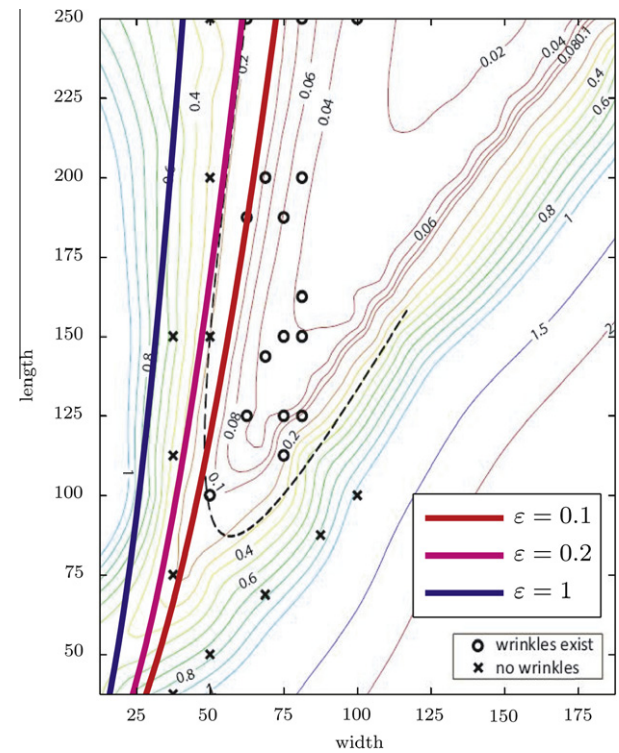

Fig. 10. Plots of the upper limits of sheet length $2L_1$ for which a configuration with 9 wrinkles can occur below an assigned strain ε of 1, 0.2 or 0.1 respectively.

where we have used the abbreviations $p = n^2 + (n + 2)^2$, $k = n^2(n + 2)^2$, and $c^2 = (48\varepsilon(1 - v^2))/(\pi^2 h^2)$. We have two inequalities (72) and (73), an upper one and a lower one. While the former provides a bound for the existence of configurations with $n + 2$

wrinkles below a prescribed strain ε for high values of the aspect ratios, the latter provides an analogous bound for low values of L_1/L_2.

In Fig. 10, the upper bound predicted by (72) for a given number of wrinkles (9 in this case, i.e. $n = 7$) has been superimposed to Fig. 9. The three plotted curves correspond to $\varepsilon = 1$, 0.2, and 0.1 respectively. Noticeably the curves are either very near or practically superimposed upon Zheng's numerical contour lines for an ample range of sheet lengths. On the other hand, our approach does not predict correctly the lower bounds observed by Zheng. This is a second indication of the fact that the present model may not be appropriate for low length-to-width aspect ratios (approximately smaller than 1.5 or even 1). In closing, our model provides an upper and a lower limit to the sheet aspect ratios for which wrinkled configurations with a given number of wrinkles can occur below a prescribed value of the applied strain. The upper limits are found to be closely comparable to similar limits obtained by Zheng (2009), while the lower limits are not.

10. Conclusion

A boundary-value problem formulated in Puntel et al. (2011) to explain the experimental results and scaling relationships obtained by Cerda et al. (2002) and by Cerda and Mahadevan (2003) has been numerically implemented using B-spline finite elements.

Cerda et al. (2002) studied wrinkling in a rectangular sheet in tension clamped along two opposite edges. Wrinkling ensues due to the hindered Poisson lateral contraction near the fixed ends. The wrinkle wavelength was measured and scaling relations for wavelength and amplitude were proposed.

The numerical implementation developed herein makes it possible to assess the role of several simplifying assumptions adopted in the analytical work by Puntel et al. (2011), namely: (1) an Ansatz on the deflection, (2) phenomenological and more easily tractable boundary conditions, and (3) the small-slope approximation used to linearize the governing equation. Numerical results include the number of wrinkles, the wrinkle wavelength, and the amplitude and critical values of the applied stretch required to induce new wrinkles in the sheet. The numerical and analytical results agree well for the full range of applied stretches, in which up to twelve wrinkles can be induced, taken into account. Though further investigation, particularly experimental, may be required, extensive comparisons of the results with experimental and numerical results available in the literature provide confirmation for the scaling laws and signal that the critical stretches may only be accurate for higher length-to-width aspect ratios.

Several limitations remain in the present approach and may be removed in future work. The model is linearly elastic and considers only moderately large deflections à la Föppl–von Kármán. Furthermore, it is based on a homogeneous tensile pre-stretch with no hindered lateral contraction near the clamps. Such flat configuration is stable for any value of the applied stretch and is currently forced to explore nontrivial wrinkled solution by the addition to the variational formulation of an appositely devised geometric constraint.

Rate-dependent behavior might well also be of interest in this context due to the usage of polyethylene in the experiments and due to the relatively high values of stretch necessary to induce large numbers of wrinkles in the sheet. For instance, using Eq. (40) with the parameter values provided in the third paragraph of Section 8, a strain of 23.5% is required for 20 wrinkles to appear.

Despite the above restrictions and the specific geometry considered, two main results emerge from the present work. First, a novel and alternative method for the analysis of wrinkling in thin sheets has been proposed and tested with positive outcome. Second, the

possibility to reliably use previously obtained closed-form solutions has been established.

References

Burton, K., Taylor, D.L., 1997. Traction forces of cytokinesis measured with optically modified elastic substrata. Nature 385, 450–454.

Cerda, E., 2005. Mechanics of scars. J. Biomech. 38, 1598–1603.

Cerda, E., Mahadevan, L., 2003. Geometry and physics of wrinkling. Phys. Rev. Lett. 90, 1–4.

Cerda, E., Ravi-Chandar, K., Mahadevan, L., 2002. Thin films: wrinkling of an elastic sheet under tension. Nature 419, 579–580.

Chung, J.Y., Chastek, T.Q., Fasolka, M.J., Ro, H.W., Stafford, C.M., 2009. Quantifying residual stress in nanoscale thin polymer films via surface wrinkling. ACS Nano 3, 844–852.

Contri, P., Schrefler, B.A., 1988. A geometrically nonlinear finite element analysis of wrinkled membrane surfaces by a no-compression material model. Commun. Appl. Numer. Methods 4, 5–15.

Embar, A., Dolbow, J., Harari, I., 2010. Imposing Dirichlet boundary conditions with Nitsche's method and spline-based finite elements. Int. J. Numer. Methods Eng. 83, 877–898.

Epstein, M., 2003. Differential equation for the amplitude of wrinkles. AIAA Journal 41, 327–329.

Fischer, F., Rammerstorfer, F., Friedl, N., Wieser, W., 2000. Buckling phenomena related to rolling and levelling of sheet metal. Int. J. Mech. Sci. 42, 1887–1910.

Friedl, N., Rammerstorfer, F.G., Fischer, F.D., 2000. Buckling of stretched strips. Comput. Struct. 78, 185–190.

Georgeu, G.A., Ross, D., 2002. Wounds and scars. Surgery 20, 139–141.

Harris, A.K., Wild, P., Stopak, D., 1980. Silicone rubber substrata a new wrinkle in the study of cell locomotion. Science 208, 177–179.

Hofer, S.O.P., Mureau, M.A.M., 2009. Improving outcomes in aesthetic facial reconstruction. Clin. Plast. Surg. 36, 345–354.

Hudson, D.A., Renshaw, A., 2006. An algorithm for the release of burn contractures of the extremities. Burns 32, 663–668.

Jenkins, C.H., Kalanovic, V.D., Padmanabhan, K., Faisal, S.M., 1999. Intelligent shape control for precision membrane antennae and reflectors in space. Smart Mater. Struct. 8, 857–867.

Kolaric, B., Vandeparre, H., Desprez, S., Vallee, R.A.L., Damman, P., 2010. In situ tuning the optical properties of a cavity by wrinkling. Appl. Phys. Lett. 96, 043119.

Laursen, T.A., 2002. Computational Contact and Impact Mechanics: Fundamentals of Modeling Interfacial Phenomena in Nonlinear Finite Element Analysis. Springer, Berlin.

Leifer, J., Belvin, W.K., 2003. Prediction of wrinkle amplitudes in thin film membranes using finite element modeling. In: 44th AIAA/ASME/ASCE/-AHS/ASC Structures, Structural Dynamics and Materials Conference, Norfolk, VA, 710 April, AIAA 2003-1983.

Liu, X., Jenkins, C.H., Schur, W.W., 2000. Fine scale analysis of wrinkled membranes. Int. J. Comput. Eng. Sci. 1, 281–298.

Lott-Crumpler, D.A., Chaudhry, H.R., 2001. Optimal patterns for suturing wounds of complex shapes to foster healing. J. Biomech. 34, 51–58.

Miller, R.K., Hedgepeth, J.M., 1982. An algorithm for finite element analysis of partly wrinkled membranes. AIAA J. 20, 1761–1763.

Miller, R.K., Hedgepeth, J.M., Weingarten, V.I., Das, P., Kahyai, S., 1985. Finite element analysis of partly wrinkled membranes. Comput. Struct. 20, 631–639.

Nayyar, V., Ravi-Chandar, K., Huang, R., 2011. Stretch-induced stress patterns and wrinkles in hyperelastic thin sheets. Int. J. Solids Struct. 48, 3471–3483.

Ohzono, T., Monobe, H., Shiokawa, K., Fujiwara, M., Shimizu, Y., 2009. Shaping liquid on a micrometre scale using microwrinkles as deformable open channel capillaries. Soft Matter 5, 4658–4664.

Piegl, L., Tiller, W., 1997. The NURBS Book. Springer, Berlin.

Puntel, E., Deseri, L., Fried, E., 2011. Wrinkling of a stretched thin sheet. J. Elast. 105, 137–170.

Stafford, C.M., Harrison, C., Beers, K.L., Karim, A., Amis, E.J., Vanlandingham, M.R., Kim, H.-C., Volksen, W., Miller, R.D., Simonyi, E., 2004. A buckling-based metrology for measuring the elastic moduli of polymeric thin films. Nat. Mater. 3, 545–550.

Steigmann, D.J., 1990. Tension-field theory. Proc. Roy. Soc. Lond. A Mater. 429, 141–173.

Tessler, A., Sleight, D.W., Wang, J.T., 2005. Effective modeling and nonlinear shell analysis of thin membranes exhibiting structural wrinkling. J. Spacecr. Rockets 42, 287–298.

Tomita, Y., Shindo, A., 1988. Onset and growth of wrinkles in thin square plates subjected to diagonal tension. Int. J. Mech. Sci. 30, 921–931.

Ueda, K., Hara, M., Okada, M., Kurokawa, N., Otani, K., Nuri, T., 2009. Lambda incision for effective tissue expansion. J. Plast. Reconstr. Aesthet. Surg.. doi:10.1016/j.bjps.2009.09.015.

Wong, Y.W., Pellegrino, S., 2006a. Wrinkled membranes PART I: experiments. J. Mech. Mater. Struct. 1, 3–25.

Wong, Y.W., Pellegrino, S., 2006b. Wrinkled membranes PART II: analytical models. J. Mech. Mater. Struct. 1, 27–61.

Wong, Y.W., Pellegrino, S., 2006c. Wrinkled membranes PART III: numerical simulations. J. Mech. Mater. Struct. 1, 63–95.

Zheng, L., 2009. Wrinkling of Dielectric Elastomer Membranes. Ph.D. Thesis. California Institute of Technology.